Paleoceanography and Paleoclimatology

RESEARCH ARTICLE
10.1029/2018PA003420

Key Points:
- CO_2 levels were relatively low (~265 ppm; $2\sigma^{+166}_{-111}$ ppm) and comparatively stable in the 500 kyr prior to and during the glaciation
- CO_2 increased by ~65 ppm during the OMT deglaciation consistent with the latest generation of ice sheet models
- The timing of the OMT glaciation is most likely controlled by both changes in CO_2 and favorable orbital forcing

Supporting Information:
- Supporting Information S1
- Table S1

Correspondence to:
R. Greenop,
rg200@st-andrews.ac.uk

Citation:
Greenop, R., Sosdian, S. M., Henehan, M. J., Wilson, P. A., Lear, C. H., & Foster, G. L. (2019). Orbital forcing, ice volume, and CO_2 across the Oligocene-Miocene transition. *Paleoceanography and Paleoclimatology*, *34*. https://doi.org/10.1029/2018PA003420

Received 22 JUN 2018
Accepted 14 JAN 2019
Accepted article online 18 JAN 2019

Orbital Forcing, Ice Volume, and CO_2 Across the Oligocene-Miocene Transition

Rosanna Greenop[1,2], Sindia M. Sosdian[3], Michael J. Henehan[4], Paul A. Wilson[1], Caroline H. Lear[3], and Gavin L. Foster[1]

[1]School of Ocean and Earth Science, National Oceanography Centre Southampton, University of Southampton, Southampton, UK, [2]School of Earth and Environmental Science, University of St Andrews, St Andrews, UK, [3]School of Earth and Ocean Sciences, Cardiff University, Cardiff, UK, [4]GFZ German Research Centre for Geosciences, Telegrafenberg, Potsdam, Germany

Abstract Paleoclimate records suggest that a rapid major transient Antarctic glaciation occurred across the Oligocene-Miocene transition (OMT; ca. 23 Ma; ~50-m sea level equivalent in 200–300 kyr). Orbital forcing has long been cited as an important factor determining the timing of the OMT glacial event. A similar orbital configuration occurred 1.2 Myr prior to the OMT, however, and was not associated with a major climate event, suggesting that additional mechanisms play an important role in ice sheet growth and decay. To improve our understanding of the OMT, we present a boron isotope-based CO_2 record between 22 and 24 Ma. This new record shows that $\delta^{11}B/CO_2$ was comparatively stable in the million years prior to the OMT glaciation and decreased by 0.7‰ (equivalent to a CO_2 increase of ~65 ppm) over ~300 kyr during the subsequent deglaciation. More data are needed, but we propose that the OMT glaciation was triggered by the same forces that initiated sustained Antarctic glaciation at the Eocene-Oligocene transition: long-term decline in CO_2 to a critical threshold and a superimposed orbital configuration favorable to glaciation (an eccentricity minimum and low-amplitude obliquity change). When comparing the reconstructed CO_2 increase with estimates of $\delta^{18}O_{sw}$ during the deglaciation phase of the OMT, we find that the sensitivity of the cryosphere to CO_2 forcing is consistent with recent ice sheet modeling studies that incorporate retreat into subglacial basins via ice cliff collapse with modest CO_2 increase, with clear implications for future sea level rise.

1. Introduction

Over the last 55 Myr, Earth's climate has gradually cooled, but superimposed upon this long-term evolution are numerous intervals of more rapid change (Zachos et al., 2008). One such example of rapid change is the glaciation that coincides with the Oligocene-Miocene stratigraphic boundary (terminology of Miller et al., 1991; ca. 23 Ma, see Figure 1). This transient cooling event is evident in the oxygen isotope record as a two-step increase in benthic foraminiferal $\delta^{18}O$ over 200–300 kyr. The magnitude of this change has typically been estimated to be approximately 1‰ and interpreted to represent a temporary expansion in continental ice volume of between 30- and 90-m sea level equivalent (Liebrand et al., 2011; Mawbey & Lear, 2013; Miller et al., 1991; Pälike, Frazier, & Zachos, 2006; Pälike, Norris, et al., 2006; Paul et al., 2000; Pekar et al., 2002). However, a recent reevaluation of stacked benthic $\delta^{18}O$ records (Mudelsee et al., 2014), alongside a new oxygen isotope record from IODP Site U1334 in the equatorial Pacific (Beddow et al., 2016), suggests that the excursion is smaller (~0.6‰) and that previous work placed too much emphasis on the extremes in the interpretation of the individual records published across the interval. Assuming the same $\delta^{18}O$ to sea level relationship as the late Pleistocene, the reevaluation of the oxygen isotope excursion suggests a sea level change of up to ~50 m (Beddow et al., 2016). Previous work has suggested $\delta^{18}O_{ice}$ may be less enriched in ^{16}O when ice sheets are smaller (e.g., Langebroek et al., 2010), which would lead to an increase in the sea level change inferred from a $\delta^{18}O_{sw}$ excursion (e.g., Edgar et al., 2007); however, this effect is likely to be a relatively minor component (15–28%) of the total $\delta^{18}O$ change during the Neogene (Gasson, Deconto, & Pollard, 2016; Gasson, Deconto, Pollard, & Levy, 2016; Langebroek et al., 2010). Slightly higher ice volume changes are estimated in a study by Liebrand et al. (2017), which uses the benthic $\delta^{18}O$ record from Site 1264 and assumptions about bottom water temperature. That study estimates that the Oligocene-Miocene transition (OMT) was associated with a change in the East Antarctic ice sheet from near–fully deglaciated to one as large as the modern day. While it is not possible to discount a Northern Hemisphere contribution to the

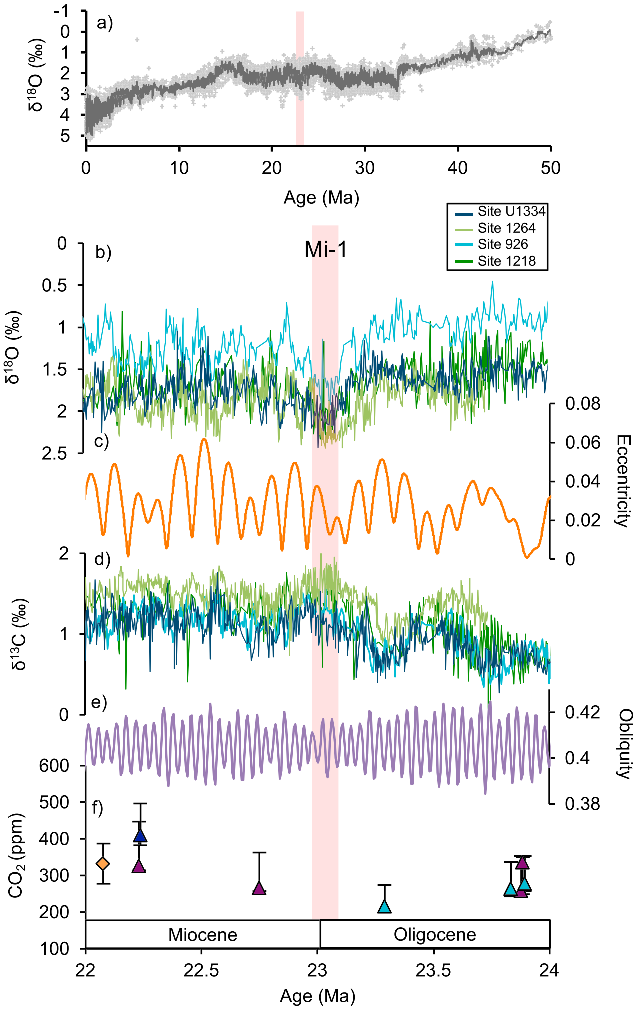

Figure 1. Climate and orbital forcing over the Oligocene-Miocene transition. (a) Cenozoic oxygen isotope composite (Zachos et al., 2008). (b) Oxygen isotope records from Site 926 (light blue; Pälike, Frazier, & Zachos, 2006), Site U1334 (dark blue; Beddow et al., 2016), Site 1264 (light green; Liebrand et al., 2011), and Site 1218 (dark green; Pälike, Norris, et al., 2006, and references therein). (c) Eccentricity orbital forcing from Laskar et al. (2004). (d) Carbon isotope records from Site 926 (light blue; Pälike, Frazier, & Zachos, 2006), Site U1334 (dark blue; Beddow et al., 2016), Site 1264 (light green; Liebrand et al., 2011), and Site 1218 (dark green; Pälike, Norris, et al., 2006, and references therein). (e) Obliquity orbital forcing from Laskar et al. (2004). (f) Previously published CO_2 records from across the Oligocene-Miocene transition glaciation. Alkenone reconstructions (light blue and purple) from Pagani et al. (2005) and (dark blue) from Zhang et al. (2013) plotted on the age model of Pagani et al. (2011) updated to Gradstein et al. (2012). Leaf stomata CO_2 reconstruction (yellow diamond) from Kürschner et al. (2008). The Oligocene-Miocene transition is highlighted in red.

continental ice budget of the OMT, despite the uncertainties in total ice volume change, Antarctica is likely to have been the main locus of ice growth at this time (DeConto et al., 2008; Naish et al., 2001).

Existing studies have shown that orbital forcing plays a key role in OMT glaciation because its timing is closely associated with the 1.2-Myr minimum in the modulation of the Earth's orbit and axial tilt (an obliquity "node"), as well as a minimum in the 400-kyr-long eccentricity cycle (i.e., a very circular orbit), both of which reduce seasonal extremes and increase the chances of winter snowfall surviving the summer ablation season (Coxall et al., 2005; Pälike, Frazier, & Zachos, 2006; Zachos, Shackleton, et al., 2001) (Figure 1). However, obliquity nodes and eccentricity minima occur regularly throughout the late Oligocene (Laskar et al., 2004), and the amplitude of the preceding node at 24.4 Ma is more extreme than the one associated with the OMT (Pälike, Frazier, & Zachos, 2006). Consequently, despite a clear orbital pacing to the OMT glaciation, changes in other boundary conditions are required to fully explain this climate perturbation (Liebrand et al., 2017).

Records of deep-ocean cooling and ice sheet expansion/retreat associated with the OMT glaciation exhibit a number of orbitally paced steps (Lear et al., 2004; Liebrand et al., 2017, 2011; Mawbey & Lear, 2013; Naish et al., 2001; Pälike, Frazier, & Zachos, 2006; Pälike, Norris, et al., 2006; Zachos, Shackleton, et al., 2001). There is a ~100-kyr periodicity throughout the OMT in a number of benthic oxygen isotope records, as well as in $\delta^{18}O_{sw}$ (calculated from paired benthic $\delta^{18}O$ and Mg/Ca measurements), which is expressed particularly clearly following the main glaciation (Beddow et al., 2016; Liebrand et al., 2011; Mawbey & Lear, 2013; Zachos, Shackleton, et al., 2001). Statistical analysis of the benthic $\delta^{18}O$ record from Ocean Drilling Program (ODP) Site 1264 across the Oligocene-Miocene suggests that the symmetry of ~100-kyr glacial-interglacial cycles changes across the OMT with a switch to more asymmetric cycles, indicative of longer-lived ice sheets that survive deeper into insolation maxima (increased ice sheet hysteresis) together with more abrupt glacial terminations after ~23 Ma (Liebrand et al., 2017).

It has also been suggested that OMT glaciation was associated with a perturbation of the carbon cycle (Mawbey & Lear, 2013; Paul et al., 2000; Zachos et al., 1997). Modeling studies (DeConto & Pollard, 2003; Gasson et al., 2012) and proxy reconstructions (e.g., Foster et al., 2012; Foster & Rohling, 2013; Greenop et al., 2014; Martínez-Botí, Foster, et al., 2015; Pagani et al., 2011; Pearson et al., 2009) both suggest that CO_2 plays an important role in controlling the timing of ice sheet expansion and retreat throughout the Cenozoic. The long-term increase of 0.8‰ in carbon isotopes from 24 to 22.9 Ma, alongside an increase in benthic foraminiferal U/Ca, has been attributed to an increase in global organic carbon burial and the associated reduction in atmospheric CO_2 (Mawbey & Lear, 2013; Paul et al., 2000; Stewart et al., 2017; Zachos et al., 1997) (Figure 1). On the basis of deep-ocean $CaCO_3$ preservation indicators and estimates of deep-ocean CO_3^{2-}, an increase in CO_2 has also been implicated as one of the driving forces of the deglaciation that followed the glacial maximum at 23 Ma (Mawbey & Lear, 2013). Yet published CO_2 records are not of sufficient temporal resolution to test these hypotheses or evaluate the presence of a CO_2 decline that would be expected to accompany an increase in organic carbon burial prior to OMT glaciation (Figure 1).

The overall OMT glaciation-deglaciation event as seen in the $\delta^{18}O$ record shows a duration of about 1 Myr and is largely symmetrical, with little evidence of ice sheet hysteresis (Beddow et al., 2016; Liebrand et al., 2011; Mawbey & Lear, 2013; Zachos, Shackleton, et al., 2001). While the first generation of Antarctic ice sheet models suggested that the CO_2 threshold for retreat of a major ice sheet was high (>1,000 ppm; Pollard & DeConto, 2005), more recent studies suggest that it is possible to simulate a more dynamic ice sheet by (i) incorporating an atmospheric component to the model to account for ice sheet-climate feedbacks, (ii) allowing for ice sheet retreat into subglacial basins via ice cliff collapse, and (iii) accounting for changes in the oxygen isotope composition of the ice sheet (Gasson, DeConto, Pollard, & Levy, 2016; Pollard et al., 2015). Based on modeling experiments for the early to mid-Miocene Antarctic ice sheet, a seawater oxygen isotope change of 0.52–0.66‰ can be simulated by changing atmospheric CO_2 between 280 and 500 ppm together with applying an astronomical configuration favorable for Antarctic deglaciation (Gasson, DeConto, Pollard, & Levy, 2016). To assess the controls on ice sheet dynamics and the potential applicability of this new generation of ice sheet models to the OMT glaciation, CO_2 data are required at substantially higher resolution than is currently available (one sample per ~500 kyr; Figure 1). Here we present a new boron isotope record with an average 50-kyr resolution across the OMT glaciation and use published $\delta^{18}O$ records to explore the relationship between ice volume and CO_2 across this interval.

2. Methods and Site Information

2.1. Site Location and Information

We utilize sediments from two open ocean drill site holes: ODP Hole 926B from Ceara Rise (3°43′N, 42°54′ W; 3,598-m water depth) in the Equatorial Atlantic Ocean and ODP Hole 872C situated in the tropical north Pacific gyre on the sedimentary cap of a flat-topped seamount (10°05.62′N, 162°52.002′E, water depth of 1,082 m). Both sites are currently located in regions where surface water is close to equilibrium (±25 ppm) with the atmosphere with respect to CO_2 (Figure 2; Takahashi et al., 2009). Age models for Sites 926 and 872 are from Pälike, Frazier, and Zachos (2006; and references therein) and Sosdian et al. (2018) updated to GTS2012 (Gradstein et al., 2012), respectively. Samples from ODP Site 926 were taken from between 469 and 522 meters composite depth (mcd) and between 110 and 117 mcd at ODP Site 872.

2.2. Boron Isotope Measurements

Trace element and boron isotope (described in delta notation as $\delta^{11}B$—permil variation from the boric acid standard SRM 951; Catanzaro et al., 1970) measurements were made on the $CaCO_3$ shells of the mixed-layer dwelling foraminifera *Globigerina praebulloides* (250–300 μm) at Site 926. At Site 872, mixed layer dwelling foraminifera *Trilobatus trilobus* (300–355 μm) was analyzed. The foraminifera were cleaned following the oxidative cleaning methodology of Barker et al. (2003) before dissolution by incremental addition of 0.5 M HNO_3. Trace element analysis was then conducted on a small aliquot of the dissolved sample at the University of Southampton using a ThermoFisher Scientific Element XR to measure Mg/Ca for ocean temperature estimates and Al/Ca to assess the competency of the sample cleaning. For boron isotope analysis, the boron was first separated from the Ca (and other trace elements) matrix using the boron specific resin Amberlite IRA 743 (Foster, 2008; Foster et al., 2013). The boron isotopic composition was then determined using a sample-standard bracketing routine on a ThermoFisher Scientific Neptune multicollector inductively coupled plasma mass spectrometer at the University of Southampton (closely following Foster et al., 2013). The uncertainty in $\delta^{11}B$ is determined from the long-term reproducibility of Japanese Geological Survey Porites coral standard following Greenop et al. (2017).

2.3. Determining pH From $\delta^{11}B$

The relationship between $\delta^{11}B_{calcite}$ and pH is very closely approximated by the following equation:

$$pH = pK_B^* - \log\left(-\frac{\delta^{11}B_{SW} - \delta^{11}B_{calcite}}{\delta^{11}B_{SW} - \alpha_B.\delta^{11}B_{calcite} - 1,000.(\alpha_B - 1)}\right), \quad (1)$$

where pK_B^* is the equilibrium constant, dependent on salinity, pressure, temperature, and seawater major ion composition (i.e., $[Ca]_{sw}$ and $[Mg]_{sw}$), α_B is the fractionation factor between the two boron species (1.0272; Klochko et al., 2006), and $\delta^{11}B_{sw}$ is the boron isotope composition of seawater. In the absence of changes in

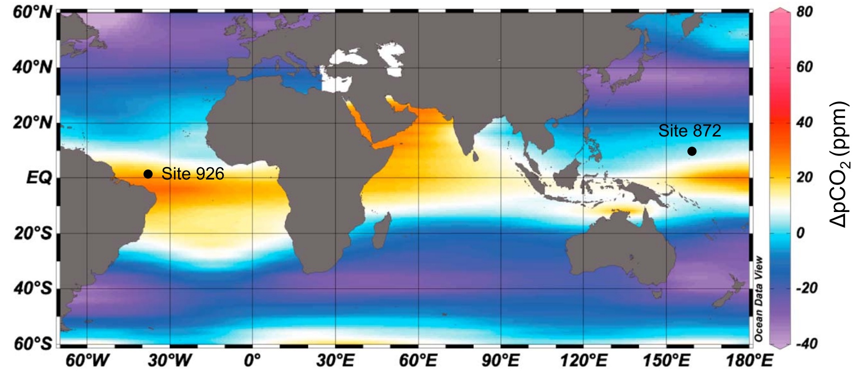

Figure 2. Map of study sites and mean annual air-sea disequilibria with respect to pCO_2. The black dots indicate the location of the sites used in this study. Ocean Drilling Program Site 926 (3°43.148′N, 42°54.507′W) is at a water depth of 3,598 m, and the modern extent of disequilibria is approximately +22 ppm. Ocean Drilling Program Site 872C (10°05.62′N, 162°52.002′E) is at a water depth of 1,082 m, and the modern extent of disequilibria is ~ 0 ppm. Data are from Takahashi et al. (2009). Plotted using Ocean Data View (Schlitzer, 2017).

the local hydrography, variations of atmospheric CO_2 have a dominant influence on pH and $[CO_2]_{aq}$ in the surface water.

2.3.1. Vital Effects

Although the $\delta^{11}B$ of foraminifera correlates well with pH and $[CO_2]_{aq}$, the $\delta^{11}B_{calcite}$ is often not exactly equal to $\delta^{11}B_{borate}$ (e.g., Foster, 2008; Henehan et al., 2013; Sanyal et al., 2001). For instance, while the pH sensitivity of $\delta^{11}B$ in modern *G. bulloides* is similar to the pH sensitivity of $\delta^{11}B$ in borate ion, the relationship between pH and $\delta^{11}B$ falls below the theoretical $\delta^{11}B_{borate}$-pH line (Martínez-Botí, Marino, et al., 2015; i.e., a lower $\delta^{11}B$ for a given pH). This effect has been attributed to the dominance, in this asymbiotic foraminifer, of respiration and calcification on the foraminifer's microenvironment, which both act to drive down local pH (Hönisch et al., 2003; Zeebe et al., 2003). In contrast, photosynthetic processes in symbiont-bearing foraminifera can cause the pH of the microenvironment to be elevated above that of the ambient seawater (Henehan et al., 2013), and the magnitude of the pH elevation determines the offset between $\delta^{11}B_{borate}$ and $\delta^{11}B_{calcite}$, which is expressed in a species-specific calibration (Henehan et al., 2016; Hönisch et al., 2003; Zeebe et al., 2003). In order to use modern calibrations further back in time, when the foraminifera were growing under different $\delta^{11}B_{sw}$, it is necessary to also correct the calibration for the $\delta^{11}B_{sw}$ to avoid overcorrecting for vital effects (see supporting information Figures S1 and S2). Here we adjust the modern calibration intercept using

$$c_{\delta^{11}B_{sw}} = c_0 + \Delta\delta^{11}B_{sw}(m_0 - 1), \tag{2}$$

where c_0 and m_0 are the intercept and slope of the calibration at modern $\delta^{11}B_{sw}$ and $\Delta\delta^{11}B_{sw}$ is the difference in $\delta^{11}B_{sw}$ between modern $\delta^{11}B_{sw}$ and the $\delta^{11}B_{sw}$ of interest (calculated from the midpoint in the OMT $\delta^{11}B_{sw}$ range; see below). Using the calibration corrected for OMT, $\delta^{11}B_{sw}$ leads to a marginally higher calculated $\delta^{11}B_{borate}$ (~0.25‰ and hence lower pCO_2) compared to the modern calibration.

At Site 872, we measure *T. trilobus* from the 300- to 350-μm size fraction and use the calibration of Sanyal et al. (2001) with a modified intercept so that it passes through the core top value for the related *T. sacculifer* (300–355 μm) from ODP 999A (Seki et al., 2010) to correct for vital effects (Sosdian et al., 2018):

$$\delta^{11}B_{borate} = \left(\delta^{11}B_{T.trilobus} - 2.69\right)/0.833. \tag{3}$$

At Site 926, *G. praebulloides* was measured from the 250- to 300-μm size fraction. Studies based on the change in $\delta^{13}C$ and $\delta^{18}O$ with size fraction have shown that at the OMT, *G. praebulloides* appears to be symbiotic (Pearson & Wade, 2009), in contrast to the asymbiotic modern *G. bulloides* that is considered to be its nearest living relative. Consequently, the modern $\delta^{11}B$-pH calibration of *G. bulloides* (Martínez-Botí, Marino, et al., 2015) is not applicable. Instead, we use the calibration for the symbiotic foraminifera *T. sacculifer*. In the absence of a *T. sacculifer* calibration for the 250- to 300-μm size fraction, we apply the same calibration as at Site 872 from Sosdian et al. (2018). We then use the close temporal overlap between the data from our two sites and with the different species to examine the validity of these vital effect assumptions.

2.3.2. Parameters for Calculating pK_B^*

Temperature changes across the Miocene-Oligocene boundary are assessed here using Mg/Ca-derived temperatures. Sea surface temperatures (SSTs) are calculated from tandem Mg/Ca analyses using the generic Mg/Ca temperature calibration of Anand et al. (2003). Adjustments were made for changes in Mg/Ca_{sw} using the records of Brennan et al. (2013) and Horita et al. (2002) and correcting for changes in dependence on Mg/Ca_{sw} following Evans and Müller (2012) using H = 0.42 calculated from *T. sacculifer* (Delaney et al., 1985; Evans & Müller, 2012; Hasiuk & Lohmann, 2010). We apply a conservative estimate of uncertainty in Mg/Ca-SST of ±3 °C (2σ), to account for analytical and calibration uncertainty, as well as uncertainty in the magnitude of the Mg/Ca_{sw} correction. The temperature effect on CO_2 calculated from $\delta^{11}B$ is ~10–15 ppm/°C; consequently uncertainty in SSTs does not significantly contribute to the final pH and CO_2 uncertainty. We assume salinity values of the same as modern day at both sites and apply a conservative estimate of ±3 psu to account for any changes in this parameter through time. Salinity has little effect on CO_2 uncertainty calculated using $\delta^{11}B$ (±3–14 ppm for a ±3‰). We use the MyAMI Specific Ion Interaction Model (Hain et al., 2015) to adjust pK_B^* for changing Mg/Ca_{sw} based on the $[Mg]_{sw}$ and $[Ca]_{sw}$ reconstructions of Brennan et al. (2013) and Horita et al. (2002) (Figure S3).

2.3.3. The Boron Isotopic Composition of Seawater ($\delta^{11}B_{sw}$)

The long residence time of boron in the oceans (~10 to 20 Myr) ensures that major changes in $\delta^{11}B_{sw}$ during our 2-Myr-long study interval are unlikely (Lemarchand et al., 2000), but it is probable that $\delta^{11}B_{sw}$ has shifted from its present value of 39.61‰ over the past 24 Myr. The $\delta^{11}B_{sw}$ during the Oligo-Miocene is therefore a large source of uncertainty and can have a significant effect on the absolute CO_2. For instance, Greenop et al. (2017) showed that the various records of $\delta^{11}B_{sw}$ diverge significantly in the early Miocene leading to large uncertainties in absolute CO_2 estimates across this interval (Sosdian et al., 2018). Here we apply a flat probability for $\delta^{11}B_{sw}$ in the range of 37.17‰ to 39.73‰ to encompass the different estimates. The minimum of this range is set to the lower 1σ uncertainty of the smoothed Greenop et al. (2017) record between 22.6 and 23.1 Ma calculated from paired planktic-benthic foraminiferal $\delta^{11}B$ and $\delta^{13}C$ analyses. The maximum extent is the average upper 1σ uncertainty of the $\delta^{11}B_{sw}$ estimates between 21.7 and 24.4 Ma from Raitzsch and Hönisch (2013) calculated from the $\delta^{11}B$ of benthic foraminifera, coupled to assumptions in past changes in CO_2, using a α_B of 1.0272 (Klochko et al., 2006). This range also encompasses the geochemical modeling estimates of $\delta^{11}B_{sw}$ from Lemarchand et al. (2000) and estimates based on the nonlinear relationship between $\delta^{11}B$ and pH alongside estimates of surface to thermocline pH gradients (Palmer et al., 1998; Pearson & Palmer, 2000) from the same time interval (Figure S3).

2.4. Estimating Absolute CO_2

To define atmospheric CO_2, a second carbonate system parameter, in addition to pH, is required. We use the regression of the Neogene dissolved inorganic carbon (DIC) estimates from Sosdian et al. (2018), where deep-ocean DIC is calculated from benthic $\delta^{11}B$ derived estimates of bottom water pH and deep-ocean carbonate ion concentration ($[CO_3^{2-}]$) constrained by the calcite compensation depth and $[Ca]_{sw}$. A linear regression is fitted through the deep-ocean DIC estimates and used to estimate changes in surface DIC relative to the modern value of 2,000 μmol/kg (Figure S3). The major source of uncertainty in the DIC estimates is the $\delta^{11}B_{sw}$ record used to calculate bottom water pH (Sosdian et al., 2018). For instance, the three $\delta^{11}B_{sw}$ record used in Sosdian et al. (2018) results in a wide range of calculated DIC estimates (e.g., 1,430 to 1,940 μmol/kg at 21.2 Ma). Consequently, to incorporate this uncertainty, we calculate absolute CO_2 using the DIC regressions determined from the three $\delta^{11}B_{sw}$ records (Sosdian et al., 2018). We undertake a full error propagation of CO_2 using a Monte Carlo simulation ($n = 10{,}000$) by perturbing each data point within the 2σ uncertainty limits in the $\delta^{11}B$ measurement (±0.16–0.85‰), SST (±3 °C), sea surface salinity (SSS; ±3 psu), $\delta^{11}B$ seawater (flat probability estimate between 37.15‰ and 39.51‰), and DIC (±378–502 μmol/kg). We then combine all the Monte Carlo simulations of CO_2 calculated using the three different DIC regressions ($n = 30{,}000$) to determine the mean and 2σ of the final CO_2 estimate (Figure S4). By using this approach, the final CO_2 estimate (and associated uncertainty) reflects the full spread of DIC estimates while utilizing the overlap in the DIC estimates calculated using different $\delta^{11}B_{sw}$ records to increase the

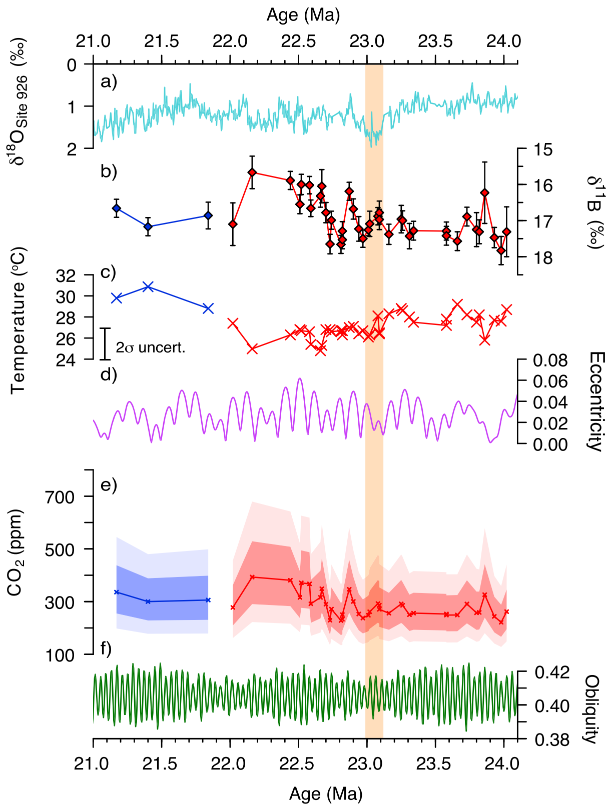

Figure 3. New Oligocene-Miocene sea surface temperature/CO_2 estimates and published climate records. (a) $\delta^{18}O$ record from Site 926 (Pälike, Frazier, & Zachos, 2006, and references therein). (b) Oligocene-Miocene transition $\delta^{11}B$ from Site 926 (red) and Site 872 (blue) from this study and Greenop et al. (2017). The data are plotted on inverted axes, and the error bars show the external reproducibility at 95% confidence. (c) Oligocene-Miocene transition Mg/Ca temperature estimates from Site 926 (red) and Site 872 (blue) from this study and Greenop et al. (2017). Temperature is calculated using the generic Mg/Ca temperature calibration of Anand et al. (2003). The 3 °C error bar reflects the 2σ temperature uncertainty that was propagated through the CO_2 calculation. (d) Eccentricity orbital forcing from Laskar et al. (2004). (e) Oligocene-Miocene transition CO_2 from Site 926 (red) and Site 872 (blue) calculated from $\delta^{11}B$ data from this study and Greenop et al. (2017). Dark and light bands show CO_2 uncertainty at the 68% and 95% confidence intervals, respectively, at Site 926 (red) and Site 872 (blue). Uncertainty was calculated using a Monte Carlo simulation (n = 30,000) including uncertainty in temperature, salinity, the DIC relationship, $\delta^{11}B_{sw}$, and the $\delta^{11}B$ measurement. See text for details of the measurement and uncertainty. (f) Obliquity orbital forcing from Laskar et al. (2004). Orange shaded area highlights the Oligocene-Miocene transition.

certainty in our CO_2 estimates. This approach results in a slight decrease in the 2σ uncertainty of the combined simulations (n = 30,000) when compared to the values obtained when using each DIC estimate in isolation. All carbonate system equilibrium constants are corrected for changes in Mg/Ca_{sw} based on the $[Mg]_{sw}$ and $[Ca]_{sw}$ reconstructions of Brennan et al. (2013) and Horita et al. (2002) following Hain et al. (2015) (Figure S3).

2.5. Estimating Relative Climate Forcing

On time scales of less than a few million years, the close relationship between pH and atmospheric CO_2 forcing means that relative pH (ΔpH) can be used to determine the relative climate forcing from CO_2 change (ΔF_{CO2}; see Hain et al., 2018, for a full discussion). The estimates of $\delta^{11}B$ seawater, DIC, SSTs, SSSs, and the $\delta^{11}B$ measurements (and the associated uncertainties) used in the calculation are the same as in sections 2.3 and 2.4; however, in analyzing ΔF_{CO2} rather than absolute CO_2 forcing, the uncertainty in the $\delta^{11}B_{sw}$ and secondary carbonate system parameter become less significant with the primary source of uncertainty originating from the $\delta^{11}B_{calcite}$ measurements (Hain et al., 2018).

ΔF_{CO2} is calculated from ΔCO_2 change using the following equation:

$$\Delta F_{CO2} = 5.32 \ln\left(\frac{C}{C_0}\right) + 0.39\left(\ln\left(\frac{C}{C_0}\right)\right)^2, \tag{4}$$

where C and C_0 are the calculated CO_2 values (Byrne & Goldblatt, 2014). Here C_0 corresponds to the oldest sample at 24.02 Ma, and the climate forcing is calculated for the rest of the record relative to this point.

3. Results and Discussion

3.1. $\delta^{11}B$ and Temperature Changes Across the OMT

Our record from *G. praebulloides* at Site 926 shows high and relatively stable $\delta^{11}B$ values (17.1 ± 0.4‰; hence the lowest CO_2) prior to and during the OMT glaciation (Figure 3). After 23 Ma, $\delta^{11}B$ decreases in a number of cycles reaching minimum values of 16.3 ± 0.5‰ at 22.5 Ma (the highest CO_2). The data from Site 872 extend the record from Site 926 between 21 and 22 Ma, and while the samples from the two sites do not overlap in the time domain, there appears to be good consistency with the data from Site 926, adding confidence to our treatment of vital effects for *G. praebulloides* at Site 926 (Figure 3). When comparing the benthic foraminiferal $\delta^{18}O$ record to our $\delta^{11}B$ data, there appears to be a decoupling between the two series in the lead up to the glaciation (Figure 3). The $\delta^{11}B$ record during this interval shows little change, whereas the $\delta^{18}O$ increases by ~0.6‰ between 23.2 and 23.1 Ma. During the deglaciation phase, however, the $\delta^{11}B$ rise broadly tracks the decrease in $\delta^{18}O$ although the $\delta^{11}B$ record shows a transient increase to pre-OMT glaciation levels around 22.8 Ma that is less pronounced in the $\delta^{18}O$ record. The $\delta^{11}B$ data from Site 872 suggest that elevated CO_2 levels are only maintained until ~22.2 Ma, after which CO_2 returns to approximately pre-OMT event values. More data are needed to determine whether the $\delta^{11}B$ change between 22.2 and 22 Ma reflects a trend in CO_2 or whether orbital-scale variations have been undersampled across this interval.

It has been widely hypothesized that a decrease in CO_2 prior to the OMT glaciation may have been one of the key triggers of the event (Mawbey & Lear, 2013; Paul et al., 2000; Zachos et al., 1997). Yet we find no evidence, within the resolution of our data, for a $\delta^{11}B$ increase (CO_2 decrease) across the benthic $\delta^{13}C$ increase that has been suggested to signify organic carbon burial in the lead-up to the OMT glaciation (Paul et al., 2000; Zachos et al., 1997). That said, the relationship between CO_2 and positive benthic $\delta^{13}C$ excursions is not always straightforward. For example, a $\delta^{13}C$ increase during the warming into the Miocene Climate Optimum coincides with a well-documented CO_2 increase (Foster et al., 2012; Greenop et al., 2014) suggesting that organic carbon burial was not the dominant control on CO_2 during that interval. Consequently, while carbon burial may occur prior to the OMT, other factors may act to keep atmospheric CO_2 levels at approximately constant levels.

The Mg/Ca-derived surface ocean temperatures at Site 926 show no clear temperature decrease during the OMT glaciation event (Figure 3), consistent with estimates of thermocline temperatures and planktic $\delta^{18}O$ estimates from the same site (Pearson et al., 1997; Stewart et al., 2017). Mg/Ca measured in thermocline dwelling *Dentoglobigerina venezuelana* at Site 926 shows no long-term change between 24.0 and 21.5 Ma, with temperature variations of less than 3 °C across the interval and no reduction in thermocline temperatures during the OMT glaciation (Stewart et al., 2017). In our new record, we see a counterintuitive multimillion year decrease in temperature of ~2 °C between 24 and 22 Myr and no clear relationship between temperature and $\delta^{18}O_{benthic}$. Temperatures decrease from ~28 °C prior to the OMT, to values comparable to modern at 23 Ma (modern 26.7 °C; Schlitzer, 2000). Several different factors could explain the lack of coherence between surface water temperature and the other proxy records such as (i) nonthermal control on Mg/Ca (e.g., salinity; e.g., Hönisch et al., 2013), (ii) variable degree of postdepositional dissolution of higher-Mg phases (Brown & Elderfield, 1996), or (iii) local influences on surface water temperature such as variability in the position of the Intertropical Convergence Zone or changes in latitudinal heat transport (Hyeong et al., 2014). The inferred temperature offset between Sites 926 and 872 may be real or attributed to the different taxa used between sites. Further work is needed at multiple sites in order to better understand the surface ocean temperature change associated with the OMT glaciation. We should stress, however, that the temperature effect on the calculation of CO_2 from $\delta^{11}B$ is relatively minor, and we propagate a large uncertainty in SSTs (3 °C; 2σ).

3.2. The Relationship Between $\delta^{11}B$ and $\delta^{18}O_{sw}$ Across the Transition at ODP Site 926

Benthic $\delta^{18}O$ is a compound record of local salinity, temperature, and global continental ice volume changes. Salinity changes in the deep sea are typically considered negligible, and therefore if an independent reconstruction of temperature can be made, the ice volume component ($\delta^{18}O_{sw}$) of the $\delta^{18}O$ record can be isolated. At ODP Site 926, a $\delta^{18}O_{sw}$ record was developed across the OMT using Mg/Ca temperature estimates from *O. umbonatus* (Mawbey & Lear, 2013). To evaluate the relationship between $\delta^{18}O_{sw}$ and $\delta^{11}B$ across this interval, we have interpolated the $\delta^{18}O_{sw}$ to our $\delta^{11}B$ age points and generated crossplots of the time equivalent data. The crossplots are based on changes in $\delta^{11}B$ and relative $\delta^{18}O_{sw}$, rather than CO_2 and ice volume, because the large uncertainties in $\delta^{11}B_{sw}$ and Mg/Ca_{sw} make it difficult to analyze the relationship between the two parameters. This treatment is appropriate because the seawater composition influences absolute values but has a negligible effect on relative changes. That said, the uncertainty of the $\delta^{11}B$ and $\delta^{18}O_{sw}$ records is still relatively large, and there are relatively few data points defining each line; therefore, these patterns should be treated as preliminary. While no relationship exists between ice volume and $\delta^{11}B/CO_2$ ($R^2 = 0.06$, p-value = 0.36) across the whole data set, when the $\delta^{18}O_{sw}/\delta^{11}B$ data points are split into peak glacial conditions (low sea level; Figure 4, blue data points) and pre/post-$\delta^{18}O$ excursion (Figure 4, red data points), the data fall along two distinct trends. The exceptions to this finding are two $\delta^{11}B$ data points from within the OMT glaciation that coincide with the maximum in eccentricity when $\delta^{18}O_{sw}$ values were similar to pre/post-OMT event conditions.

Based on the central estimates of the data available, the two different trend lines are statistically significant at the 95% confidence level and thus could reflect the different sensitivity of the ice sheet to CO_2 forcing under different orbital forcing. It is possible that the cool summers associated with low eccentricity would enable the ice sheet to expand further for a given CO_2 forcing compared to high eccentricity conditions, shifting these points from the other trend lines. Alternatively, the observed relationships could be interpreted as evidence for there being two components to the cryosphere, which respond differently for a given CO_2 forcing. Statistical analysis of a long Oligo-Miocene benthic $\delta^{18}O$ record from Walvis Ridge suggests that the OMT is characterized by more nonlinear interactions compared to other intervals with similarly high amplitude $\delta^{18}O$ change, possibly related to cryosphere changes (Liebrand et al., 2017). While we cannot identify

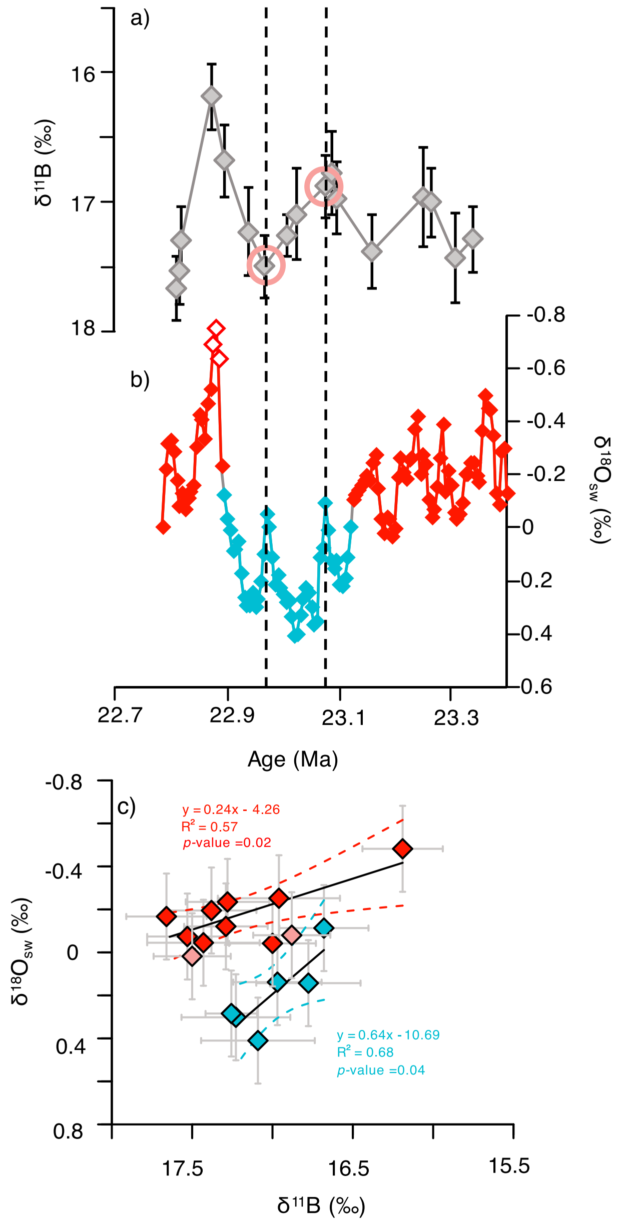

Figure 4. The relationship between $\delta^{11}B$ and $\delta^{18}O_{sw}$. (a) The $\delta^{11}B$ record from Site 926 focused on 22.7–23.4 Ma from this study and Greenop et al. (2017). The pink circles highlight $\delta^{11}B$ samples that fall within "peak glaciation conditions" but show a better fit on the pre/post-Oligocene-Miocene transition (OMT) glaciation event line (see text for details). Note the axis is reversed. (b) Relative $\delta^{18}O_{sw}$ change color-coded for peak glacial (blue) and preglacial/postglacial conditions (red; Mawbey & Lear, 2013). Open circles are $\delta^{18}O_{sw}$ estimates within the "dissolution event" and therefore bias toward negative values. The dashed black lines show the coincident timing of the two $\delta^{11}B$ data points that sit on the pre/post-OMT glaciation event line and the eccentricity paced high sea level events within the OMT glaciation. Note the inverted axis. (c) Time equivalent crossplot of $\delta^{11}B$ (error bars are external reproducibility at 95% confidence) and relative $\delta^{18}O_{sw}$ (error bars ±0.2‰). The peak glacial (blue) and pre/post-OMT glaciation (red) data plot along two separate lines. Dotted lines are the 95% confidence intervals on the fit of the linear regressions. The pink data points fall within the glacial interval (circled in (a)) but plot on the preglacial/postglacial line (see text for details).

the ice sheet that forms during the OMT glaciation, the Greenland ice sheet, the marine-based West Antarctic ice sheet, and sections of East Antarctic ice sheet have all been shown to be highly sensitive to CO_2 and orbital forcing (DeConto et al., 2008; Gasson, DeConto, Pollard, & Levy, 2016; Pollard & DeConto, 2009). While these new $\delta^{11}B$ data show some tentative evidence for both an orbital configuration and CO_2 control on ice sheet growth over the OMT, more data are clearly needed to further investigate these relationships.

3.3. ΔF_{CO2} Associated With OMT Deglaciation

To assess the significance of CO_2 in driving the OMT deglaciation phase, it is instructive to calculate the climate forcing change from the $\delta^{11}B$ data. The uncertainty in $\delta^{11}B_{sw}$ and the secondary carbonate system parameter become less significant when considering the relative change in CO_2 forcing on climate (ΔF_{CO2}) over short time scales (in this case over <1 Myr), compared to when calculating absolute CO_2 (Hain et al., 2018). To further reduce uncertainty, we estimate the ΔF_{CO2} between two time windows, identified using the $\delta^{18}O_{benthic}$ records (Pälike, Frazier, & Zachos, 2006). A comparison is made between the peak glaciation (23.1–22.9 Ma) identified from the $\delta^{18}O_{benthic}$ record and a snapshot postevent when $\delta^{18}O_{benthic}$ values have stabilized (22.7–22.2 Ma) following the post-OMT seafloor dissolution event (Mawbey & Lear, 2013). Based on this assessment, we calculate that the rebound out of the OMT glaciation was associated with a change in radiative forcing of 1.15 W/m^2 (2σ range 0.8–1.5 W/m^2). However, we note that while comparing ΔF_{CO2} between two time windows reduces the calculated uncertainty, it may also underestimate the amplitude of ΔF_{CO2} as the CO_2 change associated with the maximum change in $\delta^{18}O_{sw}$ is not captured.

Our new ΔF_{CO2} estimate can then be compared to published estimates of $\Delta\delta^{18}O_{sw}$ to investigate the sensitivity of ice to CO_2 forcing over the OMT. Combining several estimates (Beddow et al., 2016; Mawbey & Lear, 2013; Mudelsee et al., 2014), the change in $\delta^{18}O_{sw}$ associated with the ΔF_{CO2} of ~1.15 W/m^2 can be estimated at -0.41 ± 0.19‰ (Figure 5). Intriguingly, this estimate is consistent with the range in $\Delta\delta^{18}O_{sw}$ modeled for a range of CO_2 change scenarios by Gasson, DeConto, Pollard, and Levy (2016; Figure 5). In this way, our data support predictions from new-generation ice sheet models of a dynamic Antarctic ice sheet during the early Miocene that waxed and waned in response to both orbital configuration and atmospheric CO_2. However, we note that the changes in ice volume modeled by Gasson, DeConto, Pollard, and Levy (2016) require extreme orbits in favor of Antarctic deglaciation, and it is as yet unclear what effect our observed CO_2 change would cause in these models under variable or average orbital configurations. Furthermore, the resolution of our data is not sufficient to determine whether the rate and timing of CO_2 and ice volume change is strictly comparable to that used in the modeling runs of Gasson, DeConto, Pollard, and Levy (2016).

3.4. CO_2 Changes Prior to the OMT Glaciation

While more robustly determined relative change in ΔF_{CO2} is clearly instructive, absolute reconstructions of CO_2 are required to shed light on the role of atmospheric CO_2 thresholds in the initiation of the OMT glaciation. Our new $\delta^{11}B$-CO_2 data suggest that CO_2 rises from a baseline value of ~265 ppm ($2\sigma^{+166}_{-111}$ ppm) to ~325 ppm ($2\sigma^{+218}_{-138}$ ppm) following the

10.1029/2018PA003420

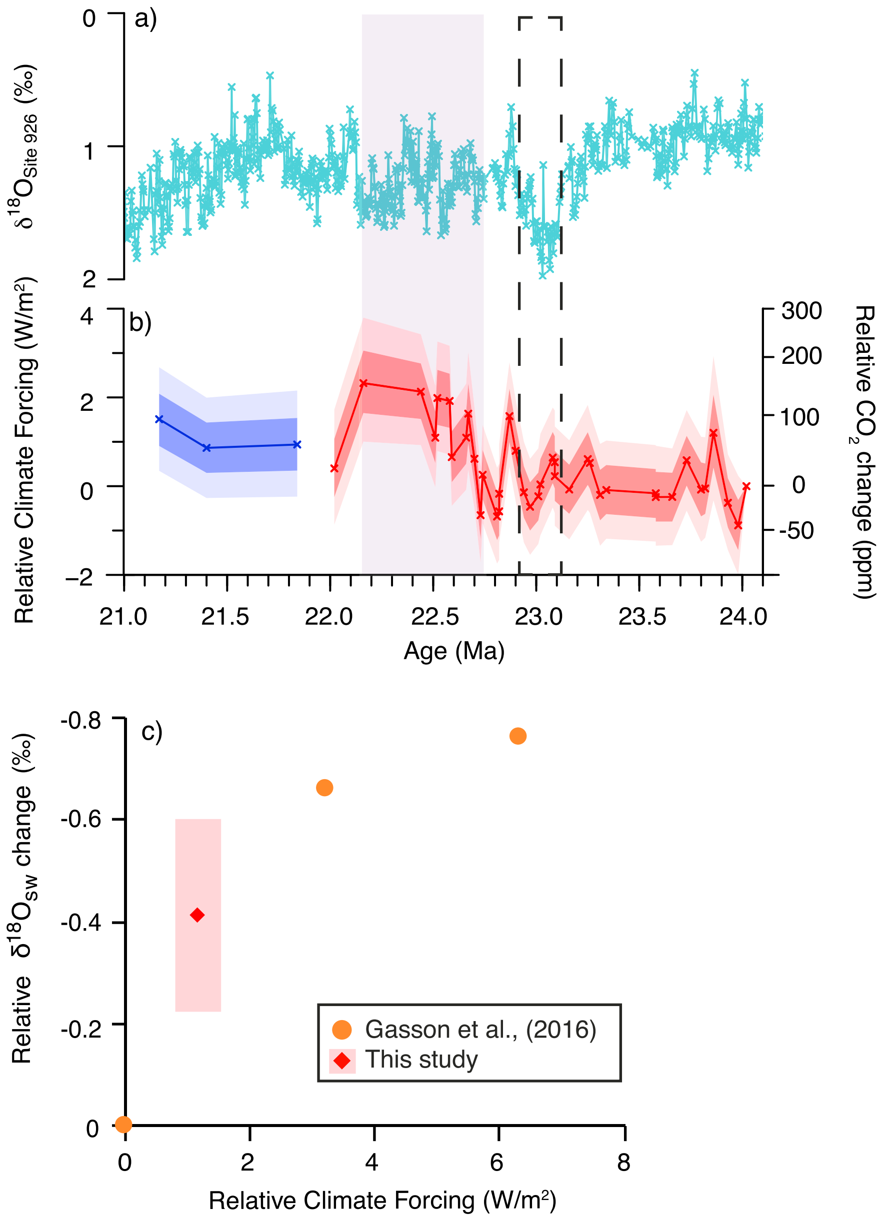

Figure 5. Oligocene-Miocene transition relative climate forcing. (a) $\delta^{18}O$ record from Site 926 (Pälike, Frazier, & Zachos, 2006 and references therein). (b) Relative climate forcing across the Oligocene-Miocene transition calculated from $\delta^{11}B$ data from this study and Greenop et al. (2017; see text for details). Dark and light bands show the uncertainty on relative climate forcing at the 68% and 95% confidence intervals, respectively, at Site 926 (red) and Site 872 (blue). All climate forcing is calculated relative to the data point at 24.02 Ma. The dashed box and grey shaded area highlight the two windows relative climate forcing is calculated from for the data in (c). In order to investigate the step change in CO_2 associated with the deglaciation, we have excluded any data within the deep-ocean dissolution event (Mawbey & Lear, 2013) between 22.9 and 22.8 Ma where $\delta^{11}B$ is highly variable. (c) Relative climate forcing (with a 95% confidence interval; red box) for data from this study plotted with an estimate of Oligocene-Miocene transition relative $\delta^{18}O_{sw}$ change (-0.41 ± 0.19‰; see text for details). The modeled CO_2 from Gasson, DeConto, and Pollard (2016) converted to relative climate forcing is also plotted with the model output $\delta^{18}O_{sw}$ and shows good agreement with our data (orange circles).

deglaciation (average CO_2 values are calculated from the postglaciation and peak glaciation windows defined in Figure 5). While the uncertainty on the CO_2 estimates is large, primarily as a result of large uncertainties on $\delta^{11}B_{sw}$ and DIC estimates (Figure S5), our data show that, within 1σ uncertainty (68% confidence interval; 200–345 ppm), CO_2 is below 400 ppm prior to and during the OMT (Figure 3). Previous estimates of CO_2 across the OMT are sparse. Nonetheless, the absolute values of CO_2

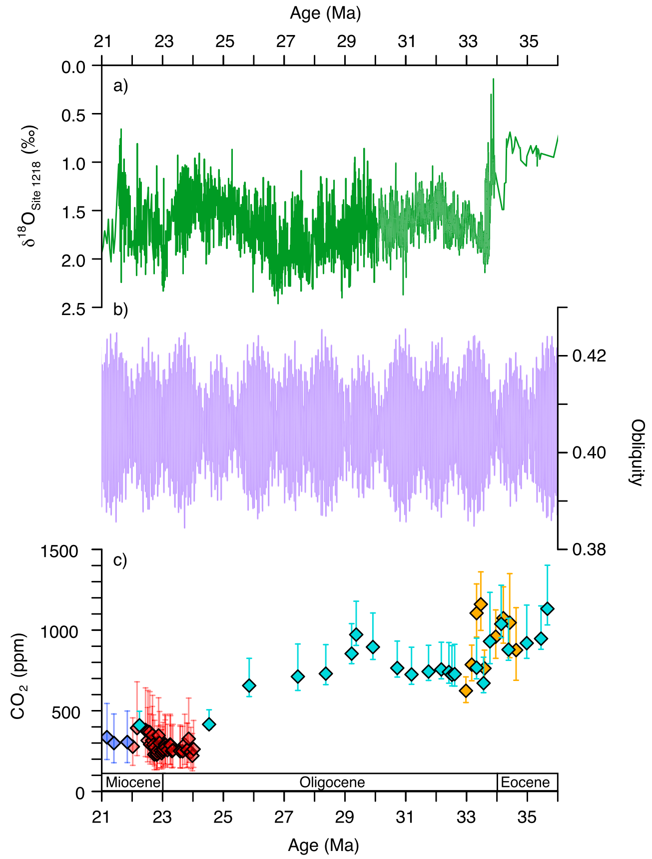

Figure 6. Long-term Oligocene climate and CO_2. (a) $\delta^{18}O$ record from Site 1218 (Pälike, Norris, et al., 2006, and references therein). (b) Obliquity orbital forcing from Laskar et al. (2004). (c) $\delta^{11}B$-CO_2 from Site 926 (calculated from $\delta^{11}B$ data from this study and Greenop et al., 2017) in red and Site 872 (this study) in dark blue, alkenone-derived CO_2 from Zhang et al. (2013) in light blue and $\delta^{11}B$-CO_2 from Pearson et al. (2009) in orange. For $\delta^{11}B$-derived CO_2 records, error bars represent 2σ uncertainty.

reconstructed here agree well with the published alkenone records of Pagani et al. (2005) and Zhang et al. (2013; when the data are plotted on the age model in Pagani et al., 2011, and updated to the Geological Timescale 2012; Gradstein et al., 2012), as well as leaf stomata CO_2 records of Kürschner et al. (2008) (Figure S6). Based on the good agreement between alkenone and boron-isotope based CO_2 records across the OMT, in Figure 6, we have plotted records derived using both methodologies to evaluate the multimillion year trends in CO_2 leading up to the OMT glaciation. The currently available data for the late Oligocene are sparse; however, it appears that the OMT glaciation occurs following a multimillion year decrease in CO_2 and when the orbital forcing was favorable for ice growth. According to our combined multiproxy data set, the CO_2 decline begins at 29.5 Ma from values of ~1,000 ppm to a minimum of ~265 ppm at 23.5 Ma (Figure 6).

A potential issue with the interpretation of a long-term late Oligocene CO_2 decrease is that the CO_2 fall between 27 and 24 Ma is at odds with the ~1‰ secular decrease in benthic $\delta^{18}O$ across the same interval, interpreted as an interval of climate warming and reduced ice volume (Mudelsee et al., 2014; Zachos, Pagani, et al., 2001). One possibility is that climate—as far as it is represented by benthic $\delta^{18}O$—and CO_2 were decoupled during the late Oligocene (as has been proposed for the Miocene; Herbert et al., 2016). A second possibility is that the relationship between Antarctic climate and deep-water temperature is not straightforward (Lear et al., 2015). For instance, a climate modeling study from the Mid-Miocene Climatic Transition suggests that the emplacement of an Antarctic ice sheet caused short-term Southern Ocean sea surface warming alongside deep-water cooling (Knorr & Lohmann, 2014). The hypothesized initiation or strengthening of the Antarctic circumpolar current during the Late Oligocene (Hill et al., 2013; Ladant et al., 2014; Lyle et al., 2007; Pfuhl & McCave, 2005) may also have resulted in large oceanographic changes, with impacts on global temperatures and benthic foraminiferal $\delta^{18}O$, although the timing of Antarctic circumpolar current development is uncertain. A third possibility is that the ice volume accommodated on Antarctica was reduced during the Late Oligocene because of the tectonic subsidence of West Antarctica below sea level (Fretwell et al., 2013; Gasson, DeConto, Pollard, & Levy, 2016; Levy et al., 2016). Indeed, tectonic subsidence and a shift to smaller marine-based ice sheets on West Antarctica during the Late Oligocene has been hypothesized to explain the long-term transition from highly symmetrical to saw-toothed $\delta^{18}O$ glacial-interglacial cycles (Liebrand et al., 2017). Finally, it is possible that the current estimates of CO_2 do not capture the full extent of the changes across this interval. More work is needed to better understand the relationship between ice volume and global climate changes of the Late Oligocene in order to give further context to the changes in CO_2, ice volume, and climate across the OMT glaciation.

4. Conclusions

The new CO_2 data presented here, when combined with published Oligocene CO_2 data, suggest that the timing of the OMT glaciation is controlled by a combination of declining CO_2 below a critical threshold and a favorable orbital configuration for ice sheet expansion on Antarctica. This combination of factors has previously been used to explain the inception of sustained Antarctic glaciation across the Eocene-Oligocene transition, potentially pointing to a common behavior of the climate system as CO_2 levels approach an ice sheet expansion threshold through the Cenozoic. Our best estimate of CO_2 suggests that values were around ~265 ppm ($2\sigma^{+166}_{-111}$ ppm) immediately prior to and during the OMT glaciation and increased by ~65 ppm during the deglaciation phase. Further work is needed, however, to gain a deeper understanding of the background climate and CO_2 conditions during the late Oligocene so that the relative contribution of the different ice sheets to the ice volume changes associated with the OMT glaciation can be better determined.

Acknowledgments
This work used samples provided by (I) ODP, which is sponsored by the U.S. National Science Foundation and participating countries under the management of Joint Oceanographic Institutions, Inc. We thank Walter Hale and Alex Wuelbers of the Bremen Core Repository for their kind assistance. The work was supported by Natural Environment Research Council (NERC) grants NE/I006176/1 (Gavin L. Foster and Caroline H. Lear), NE/I006427/1 (Caroline H. Lear), and NE/K014137/1 (Paul A. Wilson), a Royal Society Wolfson Award (Paul A. Wilson), a NERC studentship (Rosanna Greenop), and financial support from the Welsh Government and Higher Education Funding Council for Wales through the Sêr Cymru National Research Network for Low Carbon, Energy and Environment (Sindia Sosdian). Diederik Liebrand and Richard Smith are thanked for helpful comments and discussion. Matthew Cooper, J. Andy Milton, and the B-team are acknowledged for their assistance in the laboratory. All data are available as supporting information to this paper.

References

Anand, P., Elderfield, H., & Conte, M. H. (2003). Calibration of Mg/Ca thermometry in planktonic foraminifera from a sediment trap time series. *Paleoceanography*, *18*(2), 1050. https://doi.org/10.1029/2002PA000846

Barker, S., Greaves, M., & Elderfield, H. (2003). A study of cleaning procedures used for foraminiferal Mg/Ca paleothermometry. *Geochemistry, Geophysics, Geosystems*, *4*(9), 8407. https://doi.org/10.1029/2003GC000559

Beddow, H. M., Liebrand, D., Sluijs, A., Wade, B. S., & Lourens, L. J. (2016). Global change across the Oligocene-Miocene transition: High-resolution stable isotope records from IODP Site U1334 (equatorial Pacific Ocean). *Paleoceanography*, *31*, 81–97. https://doi.org/10.1002/2015PA002820

Brennan, S. T., Lowenstein, T. K., & Cendón, D. I. (2013). The major-ion composition of Cenozoic seawater: The past 36 million years from fluid inclusions in marine halite. *American Journal of Science*, *313*(8), 713–775. https://doi.org/10.2475/08.2013.01

Brown, S. J., & Elderfield, H. (1996). Variations in Mg/Ca and Sr/Ca ratios of planktonic foraminifera caused by postdepositional dissolution: Evidence of shallow Mg-dependent dissolution. *Paleoceanography*, *11*(5), 543–551. https://doi.org/10.1029/96PA01491

Byrne, B., & Goldblatt, C. (2014). Radiative forcing at high concentrations of well-mixed greenhouse gases. *Geophysical Research Letters*, *41*, 152–160. https://doi.org/10.1002/2013GL058456

Catanzaro, E. J., Champion, C., Garner, E., Marinenko, G., Sappenfield, K., & Shields, S. W. (1970). *Boric acid: Isotopic and assay standard reference materials NBS (US) special publications*. Washington, DC: National Bureau of Standards, Institute for Materials Research.

Coxall, H. K., Wilson, P. A., Palike, H., Lear, C. H., & Backman, J. (2005). Rapid stepwise onset of Antarctic glaciation and deeper calcite compensation in the Pacific Ocean. *Nature*, *433*(7021), 53–57. https://doi.org/10.1038/nature03135

DeConto, R. M., & Pollard, D. (2003). A coupled climate-ice sheet modeling approach to the Early Cenozoic history of the Antarctic ice sheet. *Palaeogeography Palaeoclimatology Palaeoecology*, *198*(1–2), 39–52. https://doi.org/10.1016/S0031-0182(03)00393-6

DeConto, R. M., Pollard, D., Wilson, P. A., Palike, H., Lear, C. H., & Pagani, M. (2008). Thresholds for Cenozoic bipolar glaciation. *Nature*, *455*(7213), 652–656. https://doi.org/10.1038/nature07337

Delaney, M. L., Be, A. W. H., & Boyle, E. A. (1985). Li, Sr, Mg and Na in foraminiferal calcite shells from laboratory culture, sediment traps, and sediment cores. *Geochimica et Cosmochimica Acta*, *49*(6), 1327–1341. https://doi.org/10.1016/0016-7037(85)90284-4

Edgar, K. M., Wilson, P. A., Sexton, P. F., & Suganuma, Y. (2007). No extreme bipolar glaciation during the main Eocene calcite compensation shift. *Nature*, *448*(7156), 908–911. https://doi.org/10.1038/nature06053

Evans, D., & Müller, W. (2012). Deep time foraminifera Mg/Ca paleothermometry: Nonlinear correction for secular change in seawater Mg/Ca. *Paleoceanography*, *27*, PA4205. https://doi.org/10.1029/2012PA002315

Foster, G., Lear, C. H., & Rae, J. W. B. (2012). The evolution of pCO_2, ice volume and climate during the middle Miocene. *Earth and Planetary Science Letters*, *341-344*, 243–254. https://doi.org/10.1016/j.epsl.2012.06.007

Foster, G. L. (2008). Seawater pH, pCO_2 and $[CO_3^{2-}]$ variations in the Caribbean Sea over the last 130 kyr: A boron isotope and B/Ca study of planktic forminifera. *Earth and Planetary Science Letters*, *271*(1–4), 254–266. https://doi.org/10.1016/j.epsl.2008.04.015

Foster, G. L., Hönisch, B., Paris, G., Dwyer, G. S., Rae, J. W. B., Elliott, T., et al. (2013). Interlaboratory comparison of boron isotope analyses of boric acid, seawater and marine $CaCO_3$ by MC-ICPMS and NTIMS. *Chemical Geology*, *358*, 1–14. https://doi.org/10.1016/j.chemgeo.2013.08.027

Foster, G. L., & Rohling, E. J. (2013). Relationship between sea level and climate forcing by CO_2 on geological timescales. *Proceedings of the National Academy of Sciences of the United States of America*, *110*(4), 1209–1214. https://doi.org/10.1073/pnas.1216073110

Fretwell, P., Pritchard, H. D., Vaughan, D. G., Bamber, J. L., Barrand, N. E., Bell, R., et al. (2013). Bedmap2: Improved ice bed, surface and thickness datasets for Antarctica. *The Cryosphere*, *7*(1), 375–393. https://doi.org/10.5194/tc-7-375-2013

Gasson, E., DeConto, R. M., & Pollard, D. (2016). Modeling the oxygen isotope composition of the Antarctic ice sheet and its significance to Pliocene sea level. *Geology*, *44*(10), 827–830. https://doi.org/10.1130/G38104.1

Gasson, E., DeConto, R. M., Pollard, D., & Levy, R. H. (2016). Dynamic Antarctic ice sheet during the early to mid-Miocene. *Proceedings of the National Academy of Sciences*, *113*(13), 3459–3464. https://doi.org/10.1073/pnas.1516130113

Gasson, E., Siddall, M., Lunt, D. J., Rackham, O. J. L., Lear, C. H., & Pollard, D. (2012). Exploring uncertainties in the relationship between temperature, ice volume, and sea level over the past 50 million years. *Reviews of Geophysics*, *50*, RG1005. https://doi.org/10.1029/2011RG000358

Gradstein, F. M., Ogg, J. G., & Schmitz, M. (2012). *The geologic time scale 2012*. Amsterdam: Elsevier.

Greenop, R., Foster, G. L., Wilson, P. A., & Lear, C. H. (2014). Middle Miocene climate instability associated with high-amplitude CO_2 variability. *Paleoceanography*, *29*, 845–853. https://doi.org/10.1002/2014PA002653

Greenop, R., Hain, M. P., Sosdian, S. M., Oliver, K. I. C., Goodwin, P., Chalk, T. B., et al. (2017). A record of Neogene seawater $\delta^{11}B$ reconstructed from paired $\delta^{11}B$ analyses on benthic and planktic foraminifera. *Climate of the Past*, *13*(2), 149–170. https://doi.org/10.5194/cp-13-149-2017

Hain, M. P., Foster, G. L., & Chalk, T. B. (2018). Robust constraints on past CO_2 climate forcing from the boron isotope proxy. *Paleoceanography and Paleoceanoclimatology*, *33*, 1099–1115. https://doi.org/10.1029/2018PA003362

Hain, M. P., Sigman, D. M., Higgins, J. A., & Haug, G. H. (2015). The effects of secular calcium and magnesium concentration changes on the thermodynamics of seawater acid/base chemistry: Implications for Eocene and Cretaceous ocean carbon chemistry and buffering. *Global Biogeochemical Cycles*, *29*, 517–533. https://doi.org/10.1002/2014GB004986

Hasiuk, F., & Lohmann, K. (2010). Application of calcite Mg partitioning functions to the reconstruction of paleocean Mg/Ca. *Geochimica et Cosmochimica Acta*, *74*(23), 6751–6763. https://doi.org/10.1016/j.gca.2010.07.030

Henehan, M. J., Foster, G. L., Bostock, H. C., Greenop, R., Marshall, B. J., & Wilson, P. A. (2016). A new boron isotope-pH calibration for Orbulina universa, with implications for understanding and accounting for 'vital effects. *Earth and Planetary Science Letters*, *454*, 282–292. https://doi.org/10.1016/j.epsl.2016.09.024

Henehan, M. J., Rae, J. W. B., Foster, G. L., Erez, J., Prentice, K. C., Kucera, M., et al. (2013). Calibration of the boron isotope proxy in the planktonic foraminifera Globigerinoides ruber for use in palaeo-CO_2 reconstruction. *Earth and Planetary Science Letters*, *364*(0), 111–122. https://doi.org/10.1016/j.epsl.2012.12.029

Herbert, T. D., Lawrence, K. T., Tzanova, A., Peterson, L. C., Caballero-Gill, R., & Kelly, C. S. (2016). Late Miocene global cooling and the rise of modern ecosystems. *Nature Geoscience*, *9*(11), 843–847. https://doi.org/10.1038/ngeo2813

Hill, D., Haywood, A., Valdes, P., Francis, J., Lunt, D., Wade, B., & Bowman, V. (2013). Paleogeographic controls on the onset of the Antarctic circumpolar current. *Geophysical Research Letters*, *40*, 5199–5204. https://doi.org/10.1002/grl.50941

Hönisch, B., Allen, K. A., Lea, D. W., Spero, H. J., Eggin, S. M., Arbuszewski, J., et al. (2013). The influence of salinity on Mg/Ca in planktic foraminifers—Evidence from cultures, core-top sediments and complementary $\delta^{18}O$. *Geochimica et Cosmochimica Acta*, *121*, 196–213. https://doi.org/10.1016/j.gca.2013.07.028

Hönisch, B., Bijma, J., Russell, A. D., Spero, H. J., Palmer, M. R., Zeebe, R. E., & Eisenhauer, A. (2003). The influence of symbiont photosynthesis on the boron isotopic composition of foraminifera shells. *Marine Micropaleontology*, *49*(1–2), 87–96. https://doi.org/10.1016/S0377-8398(03)00030-6

Horita, J., Zimmermann, H., & Holland, H. D. (2002). Chemical evolution of seawater during the Phanerozoic: Implications from the record of marine evaporites. *Geochimica et Cosmochimica Acta*, *66*(21), 3733–3756. https://doi.org/10.1016/S0016-7037(01)00884-5

Hyeong, K., Lee, J., Seo, I., Lee, M. J., Yoo, C. M., & Khim, B.-K. (2014). Southward shift of the Intertropical Convergence Zone due to Northern Hemisphere cooling at the Oligocene-Miocene boundary. *Geology*, *42*(8), 667–670. https://doi.org/10.1130/G35664.1

Klochko, K., Kaufman, A. J., Yao, W. S., Byrne, R. H., & Tossell, J. A. (2006). Experimental measurement of boron isotope fractionation in seawater. *Earth and Planetary Science Letters*, *248*(1–2), 276–285. https://doi.org/10.1016/j.epsl.2006.05.034

Knorr, G., & Lohmann, G. (2014). Climate warming during Antarctic ice sheet expansion at the Middle Miocene transition. *Nature Geoscience*, *7*(5), 376–381. https://doi.org/10.1038/ngeo2119

Kürschner, W. M., Kvaček, Z., & Dilcher, D. L. (2008). The impact of Miocene atmospheric carbon dioxide fluctuations on climate and the evolution of terrestrial ecosystems. *Proceedings of the National Academy of Sciences of the United States of America*, *105*(2), 449–453. https://doi.org/10.1073/pnas.0708588105

Ladant, J. B., Donnadieu, Y., & Dumas, C. (2014). Links between CO_2, glaciation and water flow: Reconciling the Cenozoic history of the Antarctic Circumpolar Current. *Climate Pastoralism*, *10*(6), 1957–1966.

Langebroek, P. M., Paul, A., & Schulz, M. (2010). Simulating the sea level imprint on marine oxygen isotope records during the middle Miocene using an ice sheet-climate model. *Paleoceanography*, *25*, PA4203. https://doi.org/10.1029/2008PA001704

Laskar, J., Robutel, P., Joutel, F., Gastineau, M., Correia, A. C. M., & Levrard, B. (2004). A long-term numerical solution for the insolation quantities of the Earth. *Astronomy and Astrophysics*, *428*(1), 261–285. https://doi.org/10.1051/0004-6361:20041335

Lear, C. H., Coxall, H. K., Foster, G. L., Lunt, D. J., Mawbey, E. M., Rosenthal, Y., et al. (2015). Neogene ice volume and ocean temperatures: Insights from infaunal foraminiferal Mg/Ca paleothermometry. *Paleoceanography*, *30*, 1437–1454. https://doi.org/10.1002/2015PA002833

Lear, C. H., Rosenthal, Y., Coxall, H. K., & Wilson, P. A. (2004). Late Eocene to early Miocene ice sheet dynamics and the global carbon cycle. *Paleoceanography*, *19*, PA4015. https://doi.org/10.1029/2004PA001039

Lemarchand, D., Gaillardet, J., Lewin, E., & Allegre, C. J. (2000). The influence of rivers on marine boron isotopes and implications for reconstructing past ocean pH. *Nature*, *408*(6815), 951–954. https://doi.org/10.1038/35050058

Levy, R., Harwood, D., Florindo, F., Sangiorgi, F., Tripati, R., von Eynatten, H., Gasson, E., et al., & SMS Science Team (2016). Antarctic ice sheet sensitivity to atmospheric CO_2 variations in the early to mid-Miocene. *Proceedings of the National Academy of Sciences*, *113*(13), 3453–3458. https://doi.org/10.1073/pnas.1516030113

Liebrand, D., de Bakker, A. T. M., Beddow, H. M., Wilson, P. A., Bohaty, S. M., Ruessink, G., et al. (2017). Evolution of the early Antarctic ice ages. *Proceedings of the National Academy of Sciences*, *114*(15), 3867–3872. https://doi.org/10.1073/pnas.1615440114

Liebrand, D., Lourens, L. J., Hodell, D. A., de Boer, B., van de Wal, R. S. W., & Palike, H. (2011). Antarctic ice sheet and oceanographic response to eccentricity forcing during the early Miocene. *Climate of the Past*, *7*(3), 869–880. https://doi.org/10.5194/cp-7-869-2011

Lyle, M., Gibbs, S., Moore, T., & Rea, D. (2007). Late Oligocene initiation of the Antarctic circumpolar current: Evidence from the South Pacific. *Geology*, *35*(8), 691–694. https://doi.org/10.1130/G23806A.1

Martínez-Botí, M. A., Foster, G. L., Chalk, T. B., Rohling, E. J., Sexton, P. F., Lunt, D. J., et al. (2015). Plio-Pleistocene climate sensitivity evaluated using high-resolution CO_2 records. *Nature*, *518*(7537), 49–54. https://doi.org/10.1038/nature14145

Martínez-Botí, M. A., Marino, G., Foster, G. L., Ziveri, P., Henehan, M. J., Rae, J. W. B., et al. (2015). Boron isotope evidence for oceanic carbon dioxide leakage during the last deglaciation. *Nature*, *518*(7538), 219–222. https://doi.org/10.1038/nature14155

Mawbey, E. M., & Lear, C. H. (2013). Carbon cycle feedbacks during the Oligocene-Miocene transient glaciation. *Geology*, *41*(9), 963–966. https://doi.org/10.1130/G34422.1

Miller, K. G., Wright, J. D., & Fairbanks, R. G. (1991). Unlocking the ice house—Oligocene-Miocene oxygen isotopes, eustasy, and margin erosion. *Journal of Geophysical Research*, *96*(B4), 6829–6848. https://doi.org/10.1029/90JB02015

Mudelsee, M., Bickert, T., Lear, C. H., & Lohmann, C. (2014). Cenozoic climate changes: A review based on time series analysis of marine benthic $\delta^{18}O$ records. *Reviews of Geophysics*, *52*, 333–374. https://doi.org/10.1002/2013RG000440

Naish, T. R., Woolfe, K. J., Barrett, P. J., Wilson, G. S., Atkins, C., Bohaty, S. M., et al. (2001). Orbitally induced oscillations in the East Antarctic ice sheet at the Oligocene/Miocene boundary. *Nature*, *413*(6857), 719–723. https://doi.org/10.1038/35099534

Pagani, M., Huber, M., Liu, Z., Bohaty, S., Henderiks, J., Sijp, W., et al. (2011). The role of carbon dioxide during the onset of Antarctic glaciation. *Science*, *334*(6060), 1261–1264. https://doi.org/10.1126/science.1203909

Pagani, M., Zachos, J. C., Freeman, K. H., Tipple, B., & Bohaty, S. (2005). Marked decline in atmospheric carbon dioxide concentrations during the Paleogene. *Science*, *309*(5734), 600–603. https://doi.org/10.1126/science.1110063

Pälike, H., Frazier, J., & Zachos, J. C. (2006). Extended orbitally forced palaeoclimatic records from the equatorial Atlantic Ceara Rise. *Quaternary Science Reviews*, *25*(23–24), 3138–3149. https://doi.org/10.1016/j.quascirev.2006.02.011

Pälike, H., Norris, R. D., Herrle, J. O., Wilson, P. A., Coxall, H. K., Lear, C. H., et al. (2006). The heartbeat of the Oligocene climate system. *Science*, *314*(5807), 1894–1898. https://doi.org/10.1126/science.1133822

Palmer, M. R., Pearson, P. N., & Cobb, S. J. (1998). Reconstructing past ocean pH-depth profiles. *Science*, *282*(5393), 1468–1471. https://doi.org/10.1126/science.282.5393.1468

Paul, H., Zachos, J. C., Flower, B., & Tripati, A. (2000). Orbitally induced climate and geochemical variability across the Oligocene/Miocene boundary. *Paleoceanography*, *15*(5), 471–485. https://doi.org/10.1029/1999PA000443

Pearson, P. N., Foster, G. L., & Wade, B. S. (2009). Atmospheric carbon dioxide through the Eocene-Oligocene climate transition. *Nature*, *461*(7267), 1110–1113. https://doi.org/10.1038/nature08447

Pearson, P. N., & Palmer, M. R. (2000). Atmospheric carbon dioxide concentrations over the past 60 million years. *Nature*, *406*(6797), 695–699. https://doi.org/10.1038/35021000

Pearson, P. N., Shackleton, N. J., Weedon, G. P., & Hall, M. A. (1997). Multispecies planktonic foraminifera stable isotope stratigraphy through Oligocene/Miocene boundary climatic cycles, site 926. In N. J. Shackleton, et al. (Eds.), *Proceedings of the Ocean Drilling Program, Scientific Results* (Vol. 154, pp. 441–449). College Station, TX: Ocean Drilling Program.

Pearson, P. N., & Wade, B. S. (2009). Taxonomy and stable isotope paleoecology of well-preserved planktonic foraminifera from the uppermost Oligocene of Trinidad. *Journal of Foraminiferal Research*, *39*(3), 191–217. https://doi.org/10.2113/gsjfr.39.3.191

Pekar, S. F., Christie-Blick, N., Kominz, M. A., & Miller, K. G. (2002). Calibration between eustatic estimates from backstripping and oxygen isotopic records for the Oligocene. *Geology*, *30*(10), 903–906. https://doi.org/10.1130/0091-7613(2002)030<0903:CBEEFB>2.0.CO;2

Pfuhl, H., & McCave, I. (2005). Evidence for late Oligocene establishment of the Antarctic Circumpolar Current. *Earth and Planetary Science Letters*, *235*(3–4), 715–728. https://doi.org/10.1016/j.epsl.2005.04.025

Pollard, D., & DeConto, R. M. (2005). Hysteresis in Cenozoic Antarctic ice-sheet variations. *Global and Planetary Change*, *45*(1–3), 9–21. https://doi.org/10.1016/j.gloplacha.2004.09.011

Pollard, D., & DeConto, R. M. (2009). Modelling West Antarctic ice sheet growth and collapse through the past five million years. *Nature*, *458*(7236), 329–332. https://doi.org/10.1038/nature07809

Pollard, D., DeConto, R. M., & Alley, R. B. (2015). Potential Antarctic Ice Sheet retreat driven by hydrofracturing and ice cliff failure. *Earth and Planetary Science Letters*, *412*, 112–121. https://doi.org/10.1016/j.epsl.2014.12.035

Raitzsch, M., & Hönisch, B. (2013). Cenozoic boron isotope variations in benthic foraminifers. *Geology*, *41*(5), 591–594. https://doi.org/10.1130/G34031.1

Sanyal, A., Bijma, J., Spero, H., & Lea, D. W. (2001). Empirical relationship between pH and the boron isotopic composition of *Globigerinoides sacculifer*: Implications for the boron isotope paleo-pH proxy. *Paleoceanography*, *16*(5), 515–519. https://doi.org/10.1029/2000PA000547

Schlitzer, R. (2000). Electronic atlas of WOCE hydrographic and tracer data now available. *Eos, Transactions American Geophysical Union*, *81*(5), 45.

Schlitzer, R. (2017). Ocean data view, *odv.awi.de*.

Seki, O., Foster, G. L., Schmidt, D. N., Mackensen, A., Kawamura, K., & Pancost, R. D. (2010). Alkenone and boron-based Pliocene pCO_2 records. *Earth and Planetary Science Letters*, *292*(1–2), 201–211. https://doi.org/10.1016/j.epsl.2010.01.037

Sosdian, S., Greenop, R., Hain, M. P., Foster, H. L., Pearson, P. N., & Lear, C. H. (2018). Constraining the evolution of Neogene ocean carbonate chemistry using the boron isotope pH proxy. *Earth and Planetary Science Letters*, *498*, 362–376. https://doi.org/10.1016/j.epsl.2018.06.017

Stewart, J. A., James, R. H., Anand, P., & Wilson, P. A. (2017). Silicate weathering and carbon cycle controls on the Oligocene-Miocene transition glaciation. *Paleoceanography*, *32*, 1070–1085. https://doi.org/10.1002/2017PA003115

Takahashi, T., Sutherland, S. C., Wanninkhof, R., Sweeney, C., Feely, R. A., Chipman, D. W., et al. (2009). Climatological mean and decadal change in surface ocean pCO_2, and net sea-air CO_2 flux over the global oceans. *Deep-Sea Research Part II*, *56*(11), 2075–2076. https://doi.org/10.1016/j.dsr.2009.07.007

Zachos, J., Pagani, M., Sloan, L., Thomas, E., & Billups, K. (2001). Trends, rhythms, and aberrations in global climate 65 Ma to present. *Science*, *292*(5517), 686–693. https://doi.org/10.1126/science.1059412

Zachos, J., Shackleton, N., Revenaugh, J., Palike, H., & Flower, B. P. (2001). Climate response to orbital forcing across the Oligocene-Miocene boundary. *Science*, *292*(5515), 274–278. https://doi.org/10.1126/science.1058288

Zachos, J. C., Dickens, G. R., & Zeebe, R. E. (2008). An early Cenozoic perspective on greenhouse warming and carbon-cycle dynamics. *Nature*, *451*(7176), 279–283. https://doi.org/10.1038/nature06588

Zachos, J. C., Flower, B. P., & Paul, H. (1997). Orbitally paced climate oscillations across the Oligocene/Miocene boundary. *Nature*, *388*(6642), 567–570. https://doi.org/10.1038/41528

Zeebe, R. E., Wolf-Gladrow, D. A., Bijma, J., & Hönisch, B. (2003). Vital effects in foraminifera do not compromise the use of $\delta^{11}B$ as a paleo-pH indicator: Evidence from modeling. *Paleoceanography*, *18*(2), 1043. https://doi.org/10.1029/2003PA000881

Zhang, Y. G., Pagani, M., Liu, Z. H., Bohaty, S., & DeConto, R. (2013). A 40-million-year history of atmospheric CO_2. *Philosophical Transactions of the Royal Society A: Mathematical, Physical and Engineering Sciences*, *371*, 1–20. https://doi.org/10.1098/rsta.2013.0096